ELECTRON-CLOUD SIMULATIONS FOR SPS AND LHC

F. Zimmermann, CERN, Geneva, Switzerland

Abstract

The electron cloud causes an increase in the vacuum pressure. It also induces slow multi-bunch and fast single-bunch instabilities, and, for the LHC, it significantly increases the heat load on the cryogenics system. This report describes our computer model of the electron cloud build up, presents simulation results for SPS and LHC, and investigates how the electron-cloud density can be reduced by modified fill patterns.

1 INTRODUCTION

Beam-induced multipacting was observed as a pressure rise at the CERN ISR in 1977, after installation of an aluminium test chamber [1]. Based on the ISR experience there was some concern for the LHC already in the 1980s [2]. In 1989, an instability at the KEK photon factory was attributed to an electron cloud [3, 4]. Observations at the photon factory included an increased vertical beam size, coupled oscillation, low threshold current, broad distributions of sidebands, and the inefficiency of a clearing gap. In 1996, a series of electron-cloud experiments were conducted by an IHEP-KEK collaboration at BEPC [5]. Shortly thereafter, in 1997, crash programs were launched for PEP-II [6, 7] (simulations, TiN coating of Al vacuum chamber,...) and for the LHC [8, 9, 10, 11, 12]. Since 1998-99, electron-cloud effects were seen with the LHC test beam in the SPS.

A combination of processes leads to an electron-cloud build up in the vacuum chamber, as is illustrated by the schematic in Fig. 1. Each passing bunch generates a number of primary (photo-)electrons, which are accelerated by the beam field and upon impact on the vacuum chamber generate secondary electrons. If the energy of the incident electrons is sufficiently high, the secondary emission yield is larger than one, and the number of electrons grows exponentially. The electron-cloud build up stops at a density roughly equal to the neutralization density, where the attractive force from the beam is on average balanced by the space-charge field of the electron cloud.

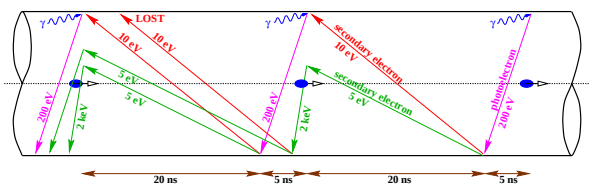

Figure 1: Schematic of electron-cloud build up in the LHC beam pipe; courtesy of F. Ruggiero [13].

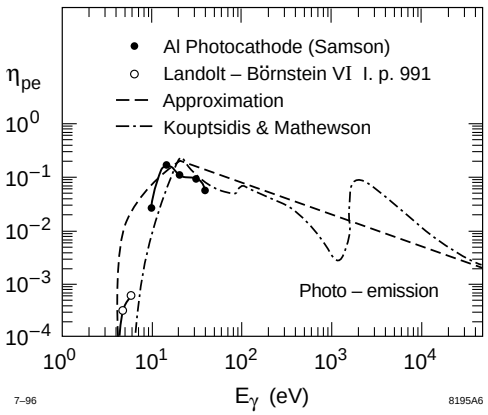

Figure 2: Measured photoemission yields for aluminium vs. photon energy; from [15, 16] and references therein.

Primary electrons are needed in order to initiate the build up of the electron cloud. In the LHC a large number of primary electrons are generated via photoemission from synchrotron radiation. The rate of incident photons is [14]

$$N_\gamma = \frac{5}{2\sqrt{3}}\alpha\gamma \ \frac{\text{photons}}{\text{radian}} \quad \text{or } 0.025 \ \frac{\text{photons}}{\text{proton meter}} \qquad (1)$$

and the critical photon energy $E_c \sim 45$ eV. Figure 2 demonstrates that at this energy the photoemission yield is close to maximum.

The photon reflectivity is another important parameter. If the reflectivity of the vacuum chamber is high, many photoelectrons are created at the top and bottom of the chamber. On the other hand, if the reflectivity is low, the majority of the photoelectrons impinges on the horizontally outward side of the vacuum chamber. In dipole magnets, these electrons do not approach the beam, and they stay at fairly low energy.

The electron yield per absorbed photon can be expressed as $Y^* = Y/(1-R) \sim 0.05$ with Y the photoelectron yield per incident photon and R the photon reflectivity. Inserting numbers [17, 18], the primary electron creation rate for the LHC is

$$\frac{d\lambda_e}{ds} \approx 10^{-3} \ \frac{\text{photo}-\text{electrons}}{\text{proton meter}}. \qquad (2)$$

In the SPS, primary electrons are generated primarily via ionisation of the residual gas. Assuming an ionization cross section σ_{ion} of 2 Mbarn, carbon monoxide gas molecules, and a pressure p of 10 nTorr, we have

$$\frac{d\lambda_e}{ds} = \frac{p}{k_B T}\sigma_{\text{ion}} \approx 6\ p[\text{Torr}] \ \frac{\text{electrons}}{\text{proton meter}} < 10^{-7} \frac{\text{electrons}}{\text{proton meter}} \qquad (3)$$

Table 1: SPS and LHC parameters

parameter	symbol	LHC	SPS
beam energy	E	7000 GeV	26 GeV
bunch population	N_b	10^{11}	5×10^{10}
rms beam sizes	σ_x	303 μm	3.0 mm
	σ_y	303 μm	2.3 mm
rms bunch length	σ_z	7.7 cm	30 cm
bunch spacing	L_{sep}	7.48 m	7.48 m
vacuum chamber 1/2 height	h_y	18 mm	22.5 mm
vacuum chamber 1/2 width	h_x	22 mm	70 mm
max. secondary emission yield	$\delta_{\max}$	1.0–2.3	≤ 2.0
reflectivity	R	2–10%	—
photo-electron yield	Y^*	0.025–0.05	—
primary yield per proton	$\frac{d\lambda_e}{ds}$	$\sim 10^{-3}$ m^{-1}	10^{-7} m^{-1}

with T the temperature and k_B Boltzmann's constant.

Table 1 compares simulation parameters for the SPS and the LHC. The vertical chamber height is almost the same.

2 MODEL

The simulation recipe is illustrated in Fig. 3. The electrons are represented by macro-particles. Typially 2000 of these are generated per bunch. Both bunches and interbunch gaps are split into slices. For each bunch slice, photoelectrons are created and existing electrons are accelerated. Whenever an electron hits the wall, it may generate secondary electrons. In the simulation, the incident macro-particle is re-emitted with a different charge. During the interbunch gap, the electrons are propagated in the magnetic field. Between gap slices, kicks are applied which model the effects of electron space charge and electron image charges.

Simulation results are:

- the energy of the lost electrons, which translates into a heat load;
- the force on a bunch behind a displaced bunch, which determines the magnitude of the multibunch wakek-field;
- the electron-cloud density near the beam, which is proportional to the growth rate of the single-bunch instability.

Figure 4 shows the actual cross section of the vacuum chamber in the LHC arcs, and the elliptical approximation, which is sometimes employed.

The photoelectrons are emitted with an initial azimuthal and energy distribution as illustrated in Figs. 5 and 6. For a reflectivity R, a fraction $(1-R)$ of the photons are unreflected. These unreflected photons are assumed to be limited to an outward cone of rms angle $11.25°$. Correspondingly, a fraction $(1-R)$ of the photoelectrons are emitted from this region. The remainder is emitted uniformly distributed around the chamber. The total azimuthal distribution is shown in Fig. 5 for two different values of R. The initial energy distribution of the photoelectrons is chosen as a Gaussian with a peak at 7 eV and rms spread of 5 eV. Since the photoelectrons are emitted at the time the generating bunch passes by, they are immediately accelerated in the beam field. Figure 6 shows the energy distribution at the moment of photoemission and the final photoelectron energy distribution at the end of the first bunch passage. The bunch imparts to an electron at the chamber wall a maximum momentum of

$$E_{\max} = 2m_0c^2 \ (N_b r_e/b)^2 \approx 200eV. \qquad (4)$$

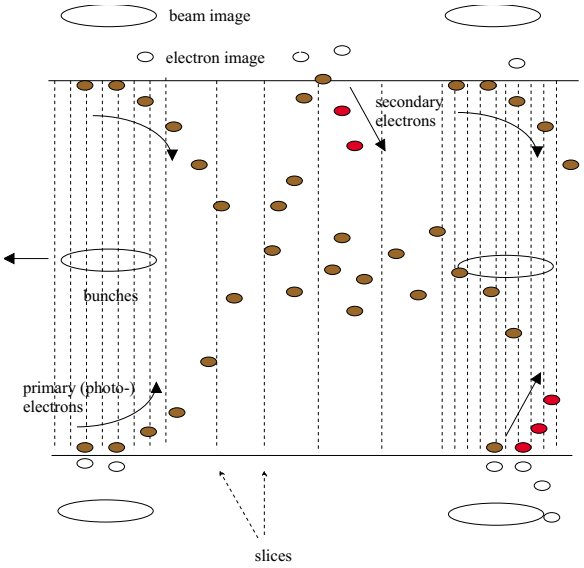

Figure 3: Schematic of simulation recipe.

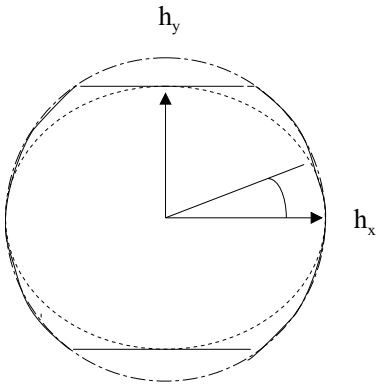

Figure 4: Transverse aperture in the LHC arcs. The solid line describes the actual cross section of the LHC beam screen. Sometimes we approximate it by the inscribed ellipse, *e.g.*, for accurate modeling of image charges.

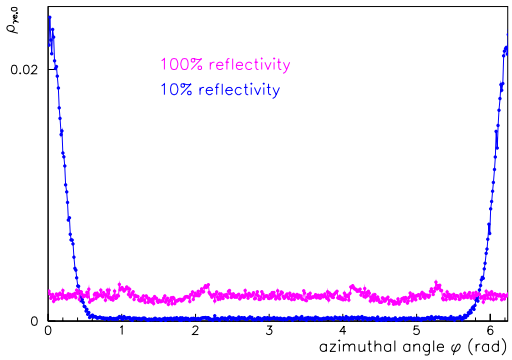

Figure 5: Initial azimuthal distribution of photoelectrons for 10% and 100% photon reflectivity.

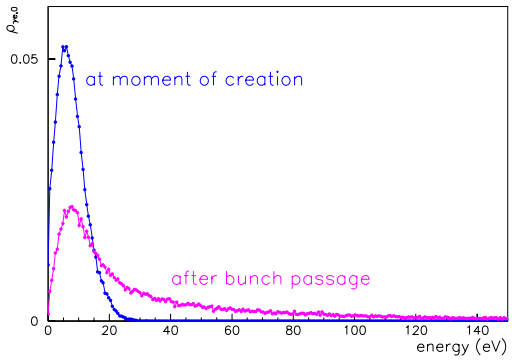

Figure 6: Initial photoelectron energy distribution at the moment of emission and after the first bunch passage.

The photoelectron emission angles ϕ and θ ($\theta > \pi/2$) are distributed randomly.

We have simulated the electron motion for a (1) drift space, (2) strong dipole field, (3) weak dipole, (4) solenoid, (5) quadrupole, (6) arbitrary fields, using a Runge-Kutta integration, and (7) wire and coaxial chambers used in laboratory multipacting tests.

In a strong (vertical) dipole field, the electron motion is constrained to the vertical direction. Here, the electron receives only a net vertical kick from the passing bunches, while the net horizontal kick is approximately zero, due to the large number of cyclotron oscillations performed during the bunch passage. For example, using LHC parameters, the number of cyclotron oscillations is about

$$\frac{eBc}{m_e c^2}\frac{2\sigma_z}{2\pi} \approx 120. \qquad (5)$$

For the SPS at 26 GeV, it is 12. The electrons spiral in the 8.4-T LHC dipole field with a typical Larmor radius $\rho = p/(eB)$ of 6μm for 200 eV electron energy, and of 26μm for 4 keV. For the SPS, the Larmor radius can be

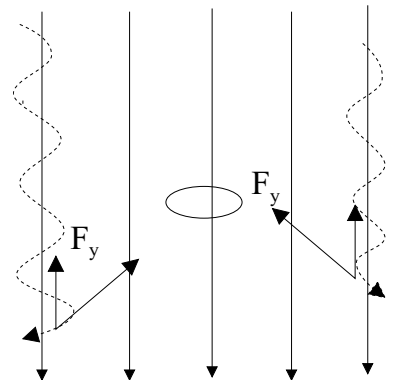

Figure 7: Schematic view of electron motion in a strong vertical dipole field. In the simulation, only a net vertical kick is applied.

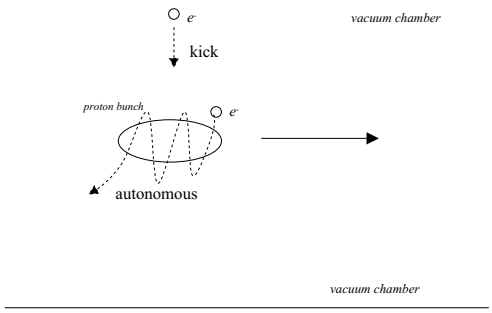

Figure 8: Electrons at large amplitudes do not move much during the bunch passage and simply receive a kick. Electrons near the bunch oscillate in the beam potential. The two situations are called 'kick region' and 'autonomous region', respectively [19].

a few hundred microns. The electron motion in a strong dipole is illustrated by a schematic in Fig. 7. The $E \times B$ longitudinal drift is ignored in the simulation.

During a bunch passage, an electron may either receive a single kick or perform many oscillations in the bunch potential, depending on its initial position, as is illustrated in Fig. 8. For each of the two limiting cases, the maximum energy transfer can be calculated, with results as shown in Fig. 9 [19].

Whenever an electron is lost to the wall, it may generate one or more secondary electrons. The average number of secondaries per incident electron is described by a universal curve, which is characterized by only two material parameters: the maximum secondary emission yield for perpendicular incidence, $\delta_{\max}$, and the energy at which the yield is maximum, $\epsilon_{\max}$.

Introducing the angle of incidence w.r.t. surface normal, θ, and the normalized electron energy $x = E_p/\epsilon_{\max}$, the analytical expression for the secondary emission yield

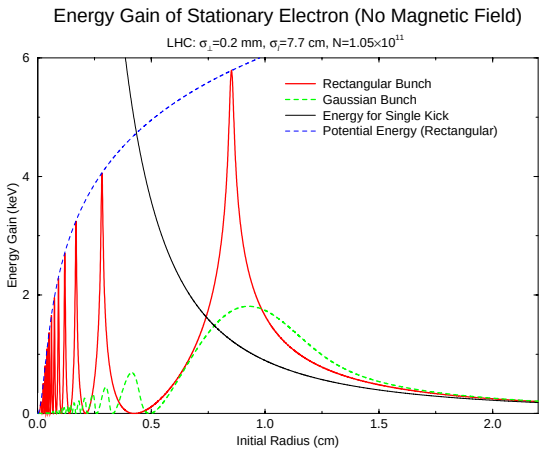

Figure 9: Maximum energy gain vs. initial particle radius for nominal LHC parameters (S. Berg). Picture taken from Ref. [19].

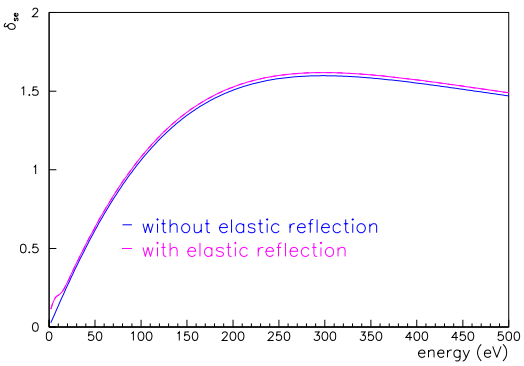

Figure 10: Secondary emission yield vs. primary electron energy E_p, for $\delta_{\max} = 1.6$ and $E_{\max} = 300$ eV with and without elastic reflection.

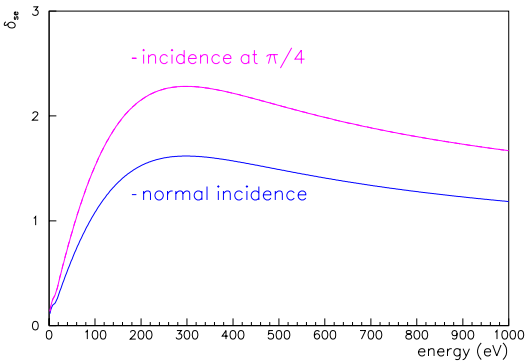

Figure 11: Secondary emission yield vs. primary electron energy E_p, for $\delta_{\max} = 1.6$ and $E_{\max} = 300$ eV for two different angles of incidence.

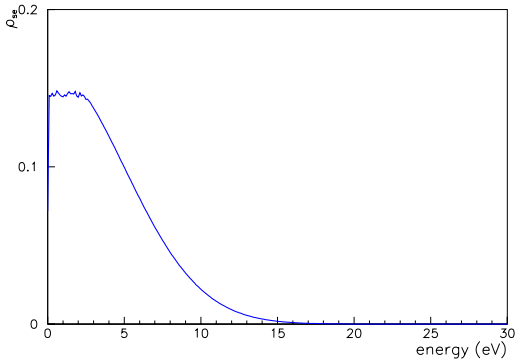

Figure 12: Initial energy distribution of secondary electrons.

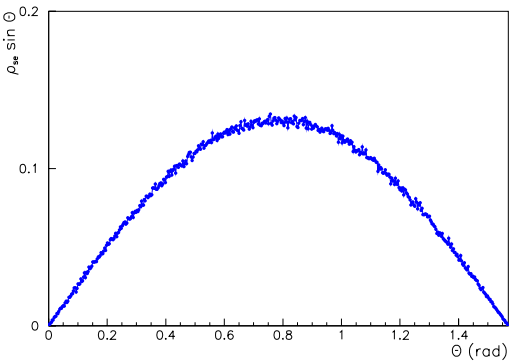

Figure 13: Initial angular distribution $dN/d\theta$ of secondary electrons vs. the polar angle θ w.r.t. surface normal.

reads [20].

$$\delta_{se}(E_p, \theta) = \delta_{\max}\ 1.11\ x^{-0.35}\ \frac{1 - e^{-2.3x^{1.35}}}{\cos\theta} \qquad (6)$$

An additional yield component represents elastic reflections of the incident electrons. This can be parametrised as [21]:

$$\delta_e(E_p) = \delta_{e,\infty} + (\hat{\delta}_e - \delta_{e,\infty})\ \exp\left(\frac{-(E_p - E_e)^2}{2\Delta^2}\right) \qquad (7)$$

with $\hat{\delta}_e = 0.1$, $\delta_{e,\infty} = 0.02$ and $\Delta = E_e = 5$ eV.

The universal curve, Eq. (6), is illustrated in Figs. 10 and 11. The second curve in Figure 10 includes the additional contribution from elastic reflections, Eq. (7).

Figures 12 and 13 depict the initial energy and angular distributions of the secondary electrons. The latter corresponds to a $\cos\theta$ distribution in spherical coordinates:

$$\frac{dN}{d\Omega} = \frac{d^2N}{d\phi\ \sin\theta\ d\theta} = \cos\theta. \qquad (8)$$

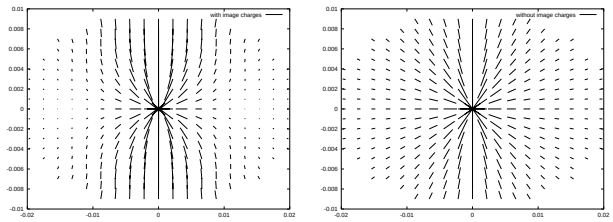

Figure 14: Electric field pattern for a beam centered in an elliptical chamber with [left] and without [right] image charges.

When plotted in intervals of θ this is weighted with the phase-space factor $\sin\theta$. Hence the density $dN/d\theta$ is maximum at $45°$.

Beam fields are calculated using the standard expression à la Bassetti-Erskine [22] or the simpler formula for round beams. An elegant expression for the field at large distances which includes the image charges in an elliptical chamber was given by Furman [23]. Denoting by $\mathcal{E} = \mathcal{E}_x + i\mathcal{E}_y$ the complex electric field, Furman's expression reads [23]

$$\mathcal{E} \approx \frac{2}{\bar{z}-\bar{z}_0} + \frac{4}{g}\sum_{n=1}^{\infty} e^{-n\mu_c}\left[\frac{\cosh n\mu_0 \cos n\phi_0}{\cosh n\mu_c} + i\,\frac{\sinh n\mu_0 \sin n\phi_0}{\sinh n\mu_c}\right]\frac{\sinh n\bar{q}}{\sinh \bar{q}} \qquad (9)$$

where $z = x+iy = g\,\cosh q = g\cosh(\mu+i\phi)$ denotes the test position, $z_0 = x_0+iy_0 = g\cosh q_0 = g\cosh(\mu_0+i\phi_0)$ the position of the source, and both $g = \sqrt{a^2-b^2}$ and $\mu_c = \tanh^{-1}(b/a)$ characterize the vacuum chamber with semi-axes a and b. In the simulation, the infinite sum is truncated at order $n = 30$.

Figure 14 shows the beam field lines in an elliptical chamber calculated with and without the beam image charges. Figures 15 and 16 depicts the horizontal and vertical electric fields for an offset beam as a function of horizontal position, again with and without including the field from the image charges. All three figures demonstrate that the image charges can significantly alter the electron motion.

Image charges of the electron cloud are also taken into account. The electron charges are assigned to points on a grid, typically consisting of 25×25 points, and the image forces are evaluated for each of the grid points. An example of the electron-cloud self field with and without image charges is shown in Fig. 17.

3 RESULTS

In this section, we discuss relevant simulation results such as: (1) electron-cloud build up for LHC and SPS, (2) transverse distribution of the electron cloud, (3) heat load for the LHC, (4) multi-bunch instability, (5) single-bunch instability, and (6) benefits of various fill patterns.

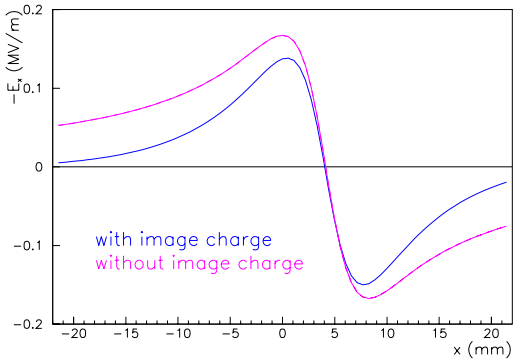

Figure 15: Horizontal electric beam field vs. horizontal position at $y = 0$ for an elliptical chamber with 22×10 mm half apertures and a beam offset of 4.3 mm in both transverse planes.

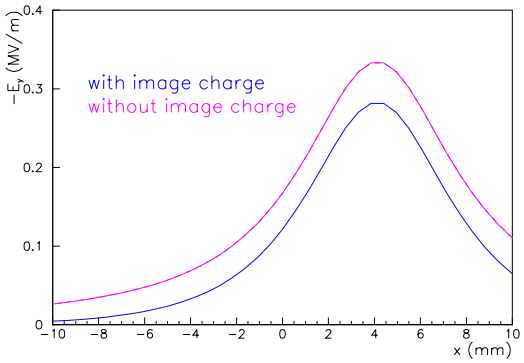

Figure 16: Vertical electric beam field vs. horizontal position at $y = 0$ for an elliptical chamber with 22×10 mm half apertures and a beam offset of 4.3 mm in both transverse planes.

Figure 18 shows that for the LHC dipole chamber the so-called critical value $\delta_{\rm crit}$ of the maximum secondary emission yield lies between 1.1 and 1.3: For the latter value, we observe an unabated growth of the electron cloud, while for the former the density of the electron cloud does not increase at all.

An analytical expression for the critical yield as a function of horizontal position x for a round aperture in a strong dipole field was derived by Stupakov [24]. It reads

$$\delta_{\rm crit}(x) = \left(\int_{-a}^{a} dy\; h(W(x,y))\frac{a}{y_0(x)}\frac{n_e(x,y,t_{sep})}{n_0(x)}\right)^{-1}, \qquad (10)$$

with a being the beam-pipe radius,

$$h(\xi) \approx 1.11\,\xi^{-0.35}\,(1-e^{-2.3\,\xi^{1.35}}) \qquad (11)$$

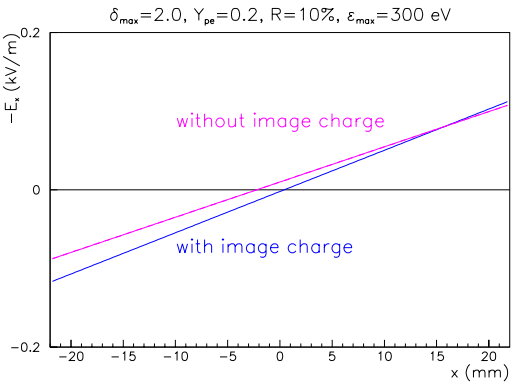

Figure 17: Horizontal electric space-charge field of electron cloud vs. horizontal position after the passage of 8 bunches in the LHC. Parameters: $\delta_{\max} = 2.0$, $Y_{pe} = 0.2$, $R = 0.1$, $\epsilon_{\max} = 300$ eV.

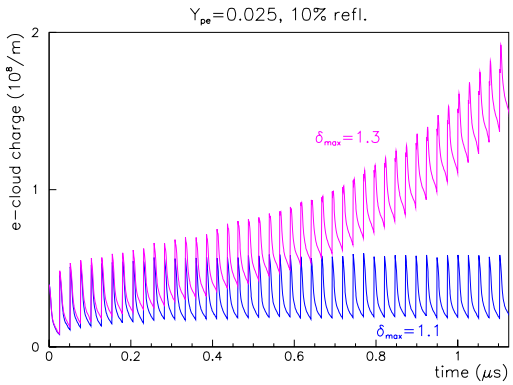

Figure 18: Electron charge per meter in an LHC dipole chamber vs. time (in s) along the bunch train. The two curves refer to $\delta_{\max} = 1.1$ and $\delta_{\max} = 1.3$. Other parameters: $\epsilon_{\max} = 450$ eV, $R = 0.1$, and $Y^* = 0.025$.

and

$$W(x,y) = \min\left(2N_b^2 r_e^2 m_e c^2 \frac{y^2}{(x^2+y^2)^2}, \Delta E_{\max}\right), \tag{12}$$

describing the energy gain of an electron at position (x, y) kicked by the beam. Here $\Delta E_{\max}$ denotes the maximum energy gain of an electron [19],

$$\Delta E_{\max} = 2m_e c^2 \frac{N_b r_e}{\sigma_z} \lambda_{\max} \ln \frac{r_c}{c_0 \sigma_\perp}, \tag{13}$$

with $c_0 \approx 1.06$, $\lambda_{\max} = 1/\sqrt{2\pi}$ for a Gaussian, $\lambda_{\max} = 1/(2\sqrt{3})$ for a rectangular distribution, $\sigma_\perp \approx \sqrt{\sigma_x \sigma_y}$, and $r_c = 2\sqrt{N_b r_e \sigma_z/(\pi \lambda_{\max})}$ is the so-called transition radius, beyond which the kick approximation applies.

The function n_e describes the electron distribution per unit length,

$$n_e(x,y,t) = \frac{a n_0(x)}{t v_s y_0(x)} \left[\lambda\left(\frac{(y-y_0)a}{t v_s y_0(x)}\right) + \lambda\left(\frac{(y-y_0)a}{t v_s y_0(x)}\right)\right], \tag{14}$$

which evolves from the initial distribution of the secondary emission, $n_0(x)$. Finally,

$$\lambda(\xi) = \frac{1}{\sqrt{2\pi}} e^{-\frac{\xi^2}{2}}, \tag{15}$$

and v_s is the characteristic velocity of the secondary electrons. For a half-Maxwellian with energy parameter E_s, we have $v_s = \sqrt{E_s/m_e}$. From Eq. (10), and ignoring the dependence of $W(x, y)$ on the beam-pipe radius a as in Ref. [25], we roughly expect that the critical yield depends on the beam pipe aperture a as $\delta_{\rm crit}(0) \sim \frac{1}{a}\, e^{-(d\,a)^2}$, with $d \approx 1/(\sqrt{2} v_s t_{\rm sep})$ and $t_{\rm sep}$ the time between bunch passages. The critical yield is minimum, or the heat load maximum, at a radius

$$a_{\max} \approx \frac{1}{d} \approx \sqrt{2} t_{\rm sep} v_s. \tag{16}$$

Numerically evaluating Eq. (10) for $x = 0$ yields the result displayed in Fig. 19. The value of the radius where the critical yield is minimum agrees reasonably well with the estimate in Eq. (16), and it scales as expected with the energy spread of the secondary electrons and with the bunch spacing.

For comparison, Fig. 20 presents the simulated critical yield. At small and moderate apertures, the agreement between the simulation and the analytical calculation is good. Both predict the minimum critical yield for a radius of about 30 mm. However, in the simulation, the critical yield decreases again, for radii exceeding 50 mm. We attribute this to electrons which survive for more than 1 bunch passage, whose contribution is not included in the analytical formula, Eq. (10).

Even for $\delta_{\max} > \delta_{\rm crit}$ the electron-cloud build up does not continue forever, but it is ultimately stopped by the repelling self-field of the electron cloud (if not by gaps in the train). Figure 21 for $\delta_{\max} = 2.3$ shows the saturation of the build up after only a few bunches, at a density of a few 10^9 per meter.

Figure 22 depicts the early stage of electron-cloud build up in the SPS, for different values of $\delta_{\max}$. Evidently, the value of the critical yield lies again between 1.1 and 1.3, *i.e.*, it is the same as for the LHC.

The electron-charge evolution over a longer time period is shown in Fig. 23, for $\delta_{\max} = 1.9$. The assumed creation rate of primary electrons corresponds to a gas pressure of about 50 nTorr. As for the LHC, the growth saturates for an electron density of a few 10^9 per meter. This saturation density is roughly consistent with the observed pressure rise [26] and with the charge deposition measured on the damper pick up [27]. A large increase in the cloud

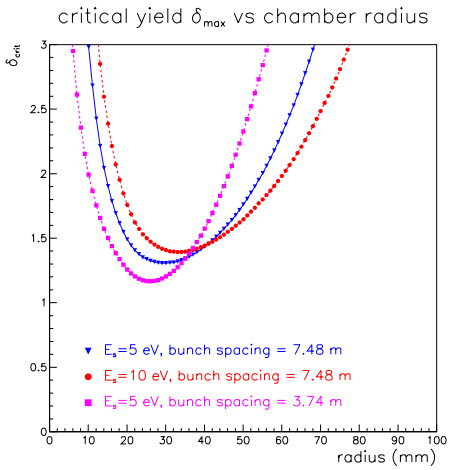

Figure 19: Critical yield as a function of chamber radius a in a dipole field, as obtained by numerical evaluation of Stupakov's formula, Eq. 10 for $x = 0$.

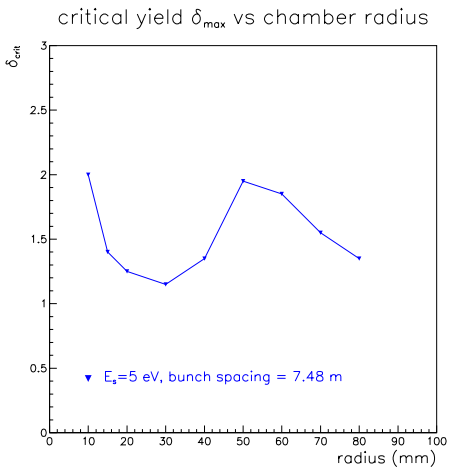

Figure 20: Simulated critical yield as a function of chamber radius a in an LHC dipole field. The three curves refer to two different values for the energy spread of the secondary electrons and two different bunch spacings, as indicated.

density occurs near the center of the 2μs-long bunch train, slowly shifting towards the head of the train as the bunch population is increased. Figures 24 and 25 present equivalent pictures for $\delta_{\max} = 1.7$ and $\delta_{\max} = 1.5$, respectively. In the latter case, the final electron-cloud blow up starts near the end of the bunch train and saturation is no longer reached. It seems that the simulation result for $\delta_{\max} = 1.9$, Fig. 23, most closely resembles the observations.

In the SPS the rate of primary electron production is proportional to the local pressure, which can change by a factor of 20–50, when the electron cloud is present. Figure 26 compares results for three different pressures— 5, 50 and 500 nTorr. The pressure dependence is rather weak. There

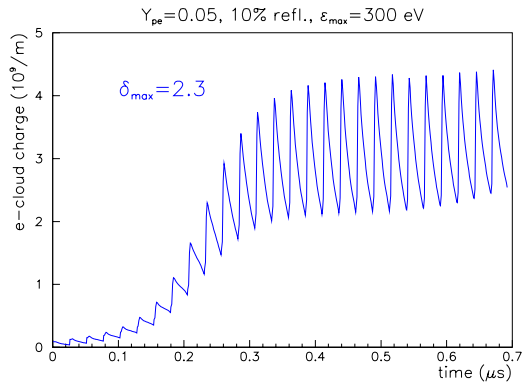

Figure 21: Electron charge per meter in an LHC dipole chamber vs. time (in 2) along bunch train for large secondary emission yield $\delta_{\max} = 2.3$. The build-up saturates due to electron-cloud space charge. Other parameters: $\epsilon_{\max} = 300$ eV, $R = 0.1$, $Y^* = 0.05$.

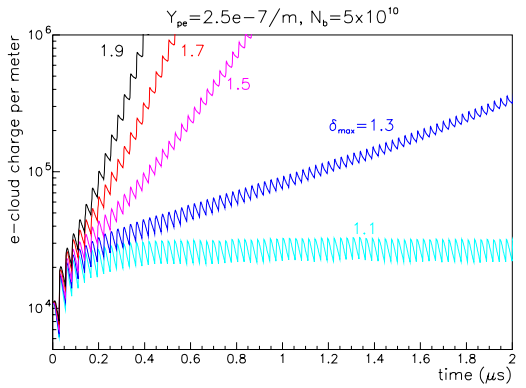

Figure 22: Electron cloud build-up in the SPS for $N_b = 5 \times 10^{10}$ and $p = 50$ nTorr. The curves refer to different values of the maximum secondary emission yield $\delta_{\max}$.

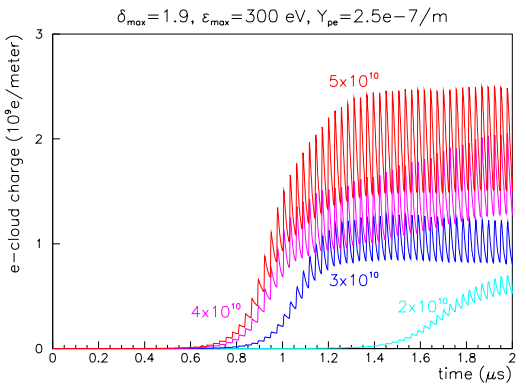

Figure 23: Electron-cloud build up in the SPS for four different bunch populations and a constant value of $\delta_{\max} = 1.9$ and $p = 50$ nTorr.

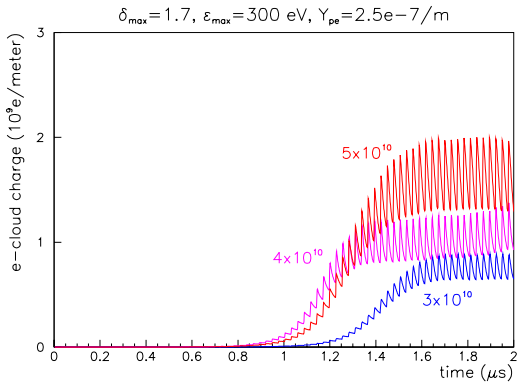

Figure 24: Electron cloud build up in the SPS for 4 different bunch populations, $\delta_{\max} = 1.7$, and $p = 50$ nTorr.

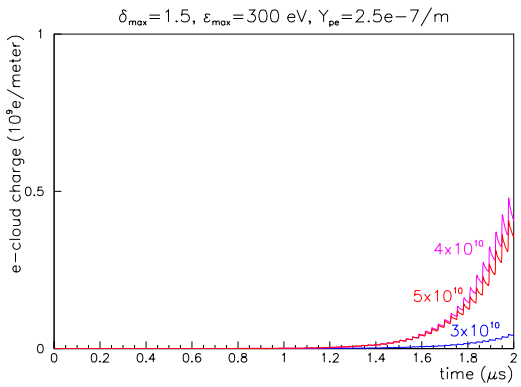

Figure 25: Electron cloud build-up in the SPS for 4 different bunch populations, $\delta_{\max} = 1.5$, and $p = 50$ nTorr.

is only a slight shift in the 'threshold position' along the bunch train.

Figures 27 and 28 compare the electron-cloud build up in the SPS with bunch spacings of 5 ns and 25 ns. For the lower bunch current, in Fig. 27, the secondary emission yield is below the critical value. In this case, the electron-cloud build up is dominated by the primary production of electrons, which is five times larger for the shorter spacing. By contrast, if at larger bunch currents the maximum emission yield exceeds the critical value, the build up of the electron cloud is more regular and much faster for the 25-ns spacing, as is shown in Fig. 28.

The electron cloud is neither concentrated around the beam nor spread out uniformly across the chamber. In the dipole magnets and, especially, if the secondary emission yield is larger than the critical yield, two vertical stripes with high electron density surround the beam, as is illustrated in Fig. 29 for the LHC and in Fig. 30 for the SPS. The two stripes represent a regions at which the average energy gain from the beam is about equal to the energy $\epsilon_{\max}$ of maximum secondary emission; compare the yield

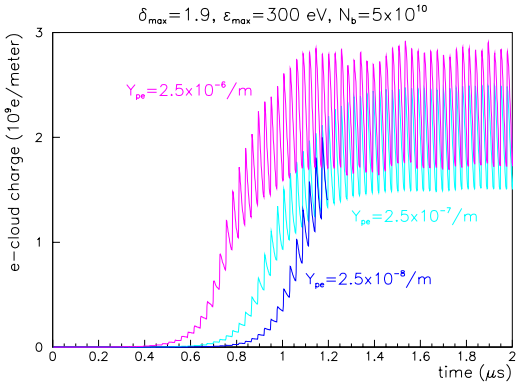

Figure 26: Electron-cloud build up in the SPS for three different rates of primary electron creation, corresponding to vacuum pressures of 5, 50 and 500 nTorr. Other parameters: $N_b = 5 \times 10^{10}$, $\epsilon_{\max} = 300$ eV, $R = 1$, $\delta_{\max} = 1.9$.

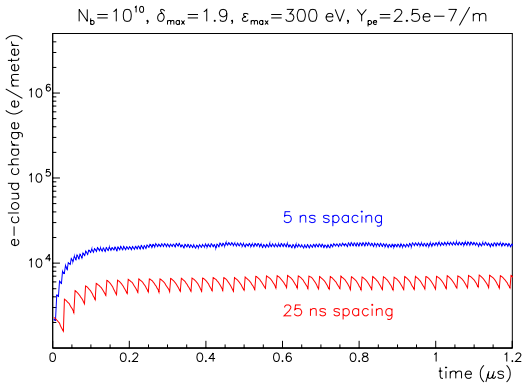

Figure 27: Electron-cloud build up in the SPS for a bunch population of $N_b = 10^{10}$, comparing bunch spacings of 5 ns and 25 ns. Other parameters: $\epsilon_{\max} = 300$ eV, $R = 1$, $\delta_{\max} = 1.9$, and $p = 50$ nTorr.

curve in Fig. 10.

For the LHC the heat load from the incident electrons is a concern. The LHC cryogenics system is designed for a maximum beam-screen heat load of about 1 W/m. Since the resistive heating by the beam and synchrotron radiation both amount to about 0.2 W/m, the average heat load due to the electron cloud must be smaller than 0.6 W/m.

Figure 31 shows the instantaneous heat load along an LHC bunch train. The various curves correspond to different values of $\delta_{\max}$. Figure 32 depicts the average heat load over the bunch train as a function of the maximum secondary emission yield. The slope of the curve increases near the critical yield $\delta_{\rm crit} \approx 1.3$.

The simulated LHC heat loads for different conditions are compiled in Table 2, for initial and final LHC parameters [28, 17, 18], *i.e.*, before and after surface conditioning due to the electron cloud.

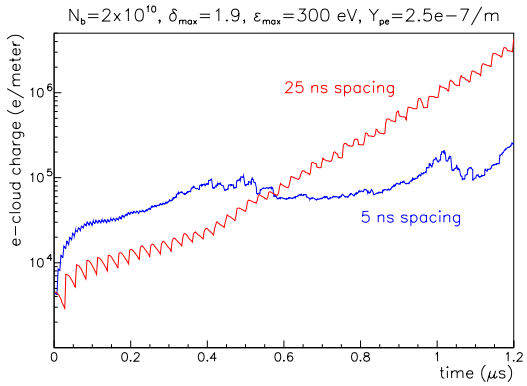

Figure 28: Electron-cloud build up in the SPS for a bunch population of $N_b = 2\times10^{10}$, comparing bunch spacings of 5 ns and 25 ns. Other parameters: $\epsilon_{\max} = 300$ eV, $R = 1$, $\delta_{\max} = 1.9$, and $p = 50$ nTorr.

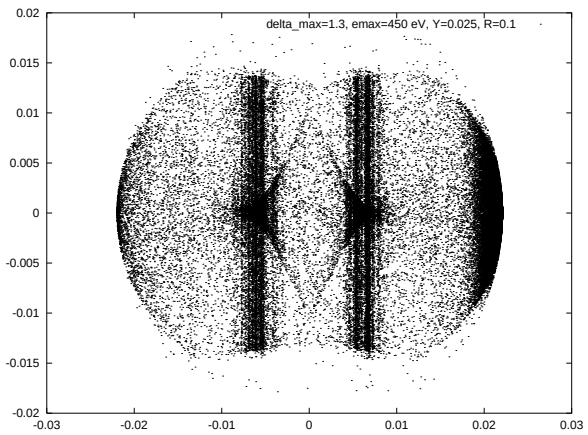

Figure 29: Snap shot of transverse electron cloud distribution in an LHC dipole chamber after 60 bunches with the design current. Vertical stripes indicate regions with large secondary emission. Parameters: $\delta_{\max} = 1.3$, $\epsilon_{\max} = 450$ eV, $R = 0.1$, and $Y^* = 0.025$.

Table 2: Simulated heat loads in LHC

magnet	initial†	final‡
arc dipole	5000 mW/m	42 mW/m
D1 dipole*	2020 mW/m	15 mW/m
(2 beams)	7580 mW/m	90 mW/m
triplet quadrupole*	14 mW/m	6 mW/m
(2 beams)	32 mW/m	14 mW/m
drift w. 3 cm radius*	7500 mW/m	460 mW/m
(2 beams)	>16000 mW/m	630 mW/m

*with transverse offsets of 4–5 millimeters.
†with $\delta_{\max} = 2.3$, $\epsilon_{\max} = 300$ eV, $Y_{pe} = 0.05$ [17, 28].
‡with $\delta_{\max} = 1.1$, $\epsilon_{\max} = 450$ eV, $Y_{pe} = 0.025$ [17, 28].

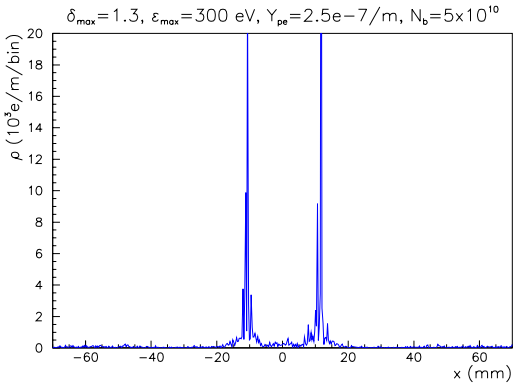

Figure 30: Projected horizontal electron charge density after 60 bunches in an SPS dipole chamber. Vertical peaks correspond to regions with large secondary emission. Parameters: $\delta_{\max} = 1.3$, $\epsilon_{\max} = 300$ eV, $R = 1$, pressure 50 nTorr, and 500 bins.

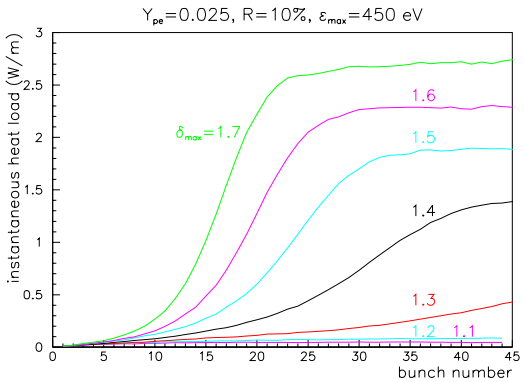

Figure 31: Instantaneous heat load in W/m vs. bunch number for LHC dipole chamber. Parameters: $\epsilon_{\max} = 450$ eV, $R = 0.1$, and $Y^* = 0.025$.

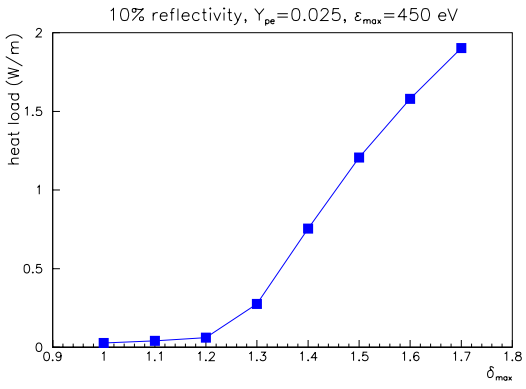

Figure 32: Heat load in LHC dipole chamber vs. maximum secondary emission yield $\delta_{\max}$. Parameters: $\epsilon_{\max} = 450$ eV, $R = 0.1$, and $Y^* = 0.025$.

If a bunch is off-set with respect to the other bunches, it will perturb the electron-cloud distribution, and the next bunch will receive an additional deflection caused by this perturbation. Thus, similar to a multibunch wake field, the electron cloud couples motion of subsequent bunches. The response of the electron cloud to a displaced bunch is illustrated in Fig. 33.

The simulation computes the effective wake field as follows. After a stationary cloud is established, one of the bunches is displaced transversely by an amount Δx or Δy. Then, we calculate the kick that the disturbed e^- cloud exerts on the next bunch. This yields an estimate of the bunch-to-bunch dipole wake field $W_1(L_{sep})$:

$$W_1(L_{sep}) = \sum_i \frac{2y_i Q_i}{N_b r_i^2(\Delta y)} \left(1 - \exp\left(-\frac{r_i^2}{2\sigma^2}\right)\right) \frac{C}{l_b}, \tag{17}$$

where $r_i = (x_i^2 + y_i^2)^{1/2}$, C is the ring circumference, l_b is the simulated length of bending magnet, and Q_i denotes the charge of the ith macro-electron.

To obtain the growth rate, we assume that the ring is uniformly filled with M bunches and that the wake of the electron cloud decays rapidly and only couples subsequent bunches. Then the complex frequency shift of μth mode is given by [29]

$$\Omega^{(\mu)}_{y\ (x)} - \omega_{\beta,y\ (x)} = \frac{N_b r_p c^2}{2\gamma C \omega_\beta} W_{1,y\ (x)} e^{i2\pi(\mu + Q_{y\ (x)})/M} \tag{18}$$

and the rise time for the fastest growing mode is

$$\tau \approx \frac{4\pi\gamma Q_{y\ (x)}}{N_b r_p c W_{1,y\ (x)}} \tag{19}$$

If the ring is not uniformly filled and there are clearing gaps, the growth is not exponential but

$$y_n \sim \frac{1}{n!}(t/\tau)^n\ \hat{y}_0 \tag{20}$$

for the nth bunch in a train. The parameter τ is exactly the same as the exponential growth time for the uniform fill, which was given above.

Figure 34 shows estimates of horizontal and vertical growth rates in the LHC as a function of the maxium secondary emission yield $\delta_{\max}$. The instability is slow, with rise times longer than 1 second. We expect that it is Landau damped by the natural intra-bunch tune spread.

The electron cloud can also act as a short-range wake field and drive a single bunch instability. Such type of instability could be responsible for the vertical emittance blow up that is observed at the KEK B factory [30], and possibly also for that in the SPS. A schematic of this instability is depicted in Fig. 35.

An approximate expression for the growth rate is [30, 31]:

$$\frac{1}{\tau} \approx 4\pi n_{\rm cloud} \frac{N_b^{1/2} r_e^{1/2} r_p \sigma_z^{1/2} \sigma_x \beta_y c}{\gamma \sigma_y^{1/2} (\sigma_x + \sigma_y)^{3/2}} \tag{21}$$

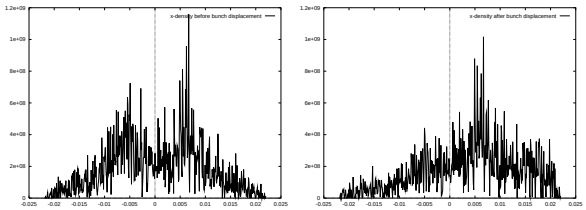

Figure 33: Projected horizontal electron charge density in an LHC bending magnet before the 41st bunch in the train is horizontally displaced by 1 cm [left] and just prior to the arrival of the 42nd bunch [right] [8]. The horizontal axis is in units of meters; the vertical coordinate is the charge (in units of e) per bin and per grid point. Other parameters: 500 grid points, $\delta_{\max} = 1.7$, $R = 1$, $Y^* = 1$.

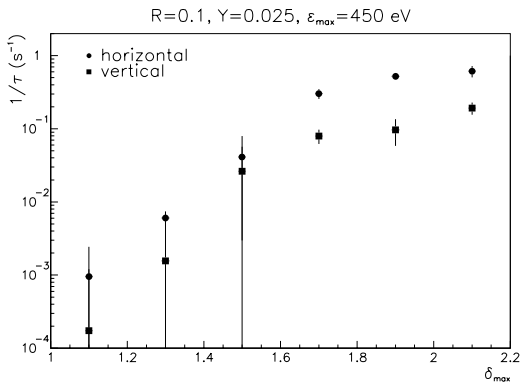

Figure 34: Multibunch instability growth rate as a function of maximum secondary emission yield $\delta_{\max}$ for the LHC. Other parameters: $\epsilon_{\max} = 450$ eV, $R = 10\%$, and $Y_{pe} = 0.025$.

It is proportional to the electron-cloud density $n_{\rm cloud}$ and also depends on a number of beam parameters, such as the bunch length. As for the fast beam-ion instability the growth is quasi-exponential, and the amplitude increases as $y \sim \exp\sqrt{t/\tau}$.

Inserting typical parameters for SPS and LHC, we find

$$\frac{1}{\tau}\,[\mathrm{s}^{-1}] \approx \begin{cases} 2\times 10^{-8}\ n_{\rm cloud}[\mathrm{m}^{-3}] & \text{SPS at 26 GeV} \\ 6\times 10^{-10}\ n_{\rm cloud}[\mathrm{m}^{-3}] & \text{LHC at 450 GeV} \\ 1\times 10^{-10}\ n_{\rm cloud}[\mathrm{m}^{-3}] & \text{LHC at 7 TeV} \end{cases}$$

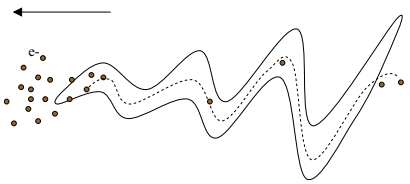

Figure 35: Illustration of a single-bunch instability driven by the electron cloud.

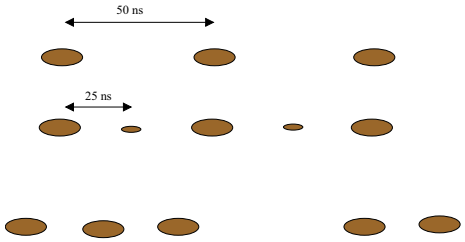

Figure 36: Double bunch spacing or gaps in the LHC train.

where $n_{\rm cloud}$ denotes the electron density near the beam.

For example, in the case of the SPS and assuming a density of $n_{\rm cloud} \approx 10^{11}$ m^{-3}, the growth rate is $\tau \approx 500$ μs.

A similar instability can occur without the electron cloud, simply due to the ionization electrons created by the bunch itself [31]. The growth time for this latter instability is proportional to the vacuum pressure. At 10 nTorr carbon monoxide pressure, we estimate $\tau \approx 50$ ms.

The growth rate of the electron-driven single-bunch instabilities may be modified by synchrotron oscillations and head-tail effects. Therefore, it should be sensitive to the rf voltage and chromaticity.

Various cures have been proposed to suppress the build up of the electron cloud. Such cures are important for the LHC start up, when the secondary emission yield is still high and an extended period of surface conditioning may be required. A promising scheme is to increase the bunch spacing, or to introduce additional gaps in the bunch train, as is shown schematically in Fig. 36.

Let us first look at the improvement that can be attained by doubling the bunch spacing. As an option we include the possibility of lower-intensity intermediate bunches (at the nominal 25 ns spacing). The purpose of these intermediate bunches is to ensure luminosity in all 4 LHC experiments, including the asymmetrically placed LHC-B.

Figure 37 shows the heat load deposited in an LHC dipole magnet as a function of intensity in the intermediate bunches, for a main-bunch separation of 50 ns and a secondary emission yield of $\delta_{\rm max} = 1.9$. The left side of the figure corresponds to the 50-ns double spacing, the right side to the nominal 25-ns spacing. The figure demonstrates that intermediate bunches with an intensity ratio up to 20% can be tolerated.

Figure 38 shows a similar picture for an SPS dipole, where now the charge of the electron cloud after the passage of 60 bunches is plotted as a function of the intensity in the intermediate bunches. The secondary emission yield is again $\delta_{\rm max} = 1.9$, which appears to describe well the present situation in the SPS.

As an alternative to doubling the bunch spacing, a second possibility to counteract the electron cloud is to add gaps between shorter bunch train segments. Several promising fill patterns are easily produced in the SPS, such as fills with 4 missing bunches between 8-bunch train sections, or 12 missing bunches after 36 bunches.

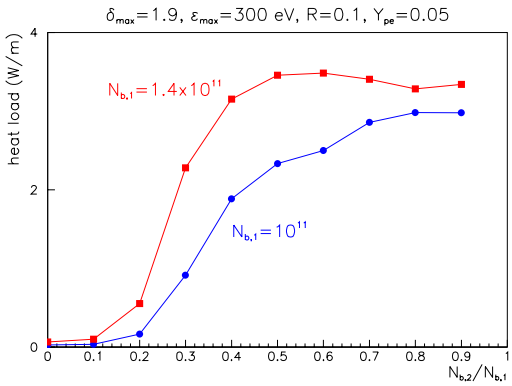

Figure 37: Heat load in an LHC dipole for twice the nominal bunch spacing and intermediate low-current bunches as a function of charge ratio $N_{b,2}/N_{b,1}$, for 2 values of $N_{b,1}$. $\epsilon_{\rm max} = 300$ eV, photon reflectivity $R = 10\%$, $\delta_{\rm max} = 1.9$, and $Y_{pe} = 0.05$.

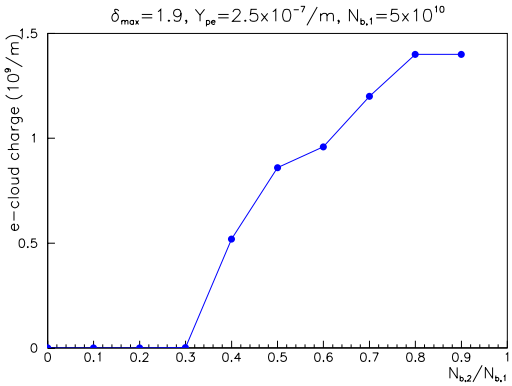

Figure 38: Electron-cloud charge in the SPS after bunch no. 60 for twice the nominal bunch spacing and intermediate low-current bunches as a function of charge ratio $N_{b,2}/N_{b,1}$ for $N_{b,1} = 5 \times 10^{10}$, $\delta_{\rm max} = 1.9$, and $p = 50$ nTorr.

Figure 39 shows the reduction of heat load with six 4-bunch gaps along the nominal 72-bunch LHC train. The heat load reduction obtained by this scheme for various values of $\delta_{\rm max}$. is summarised in Table 3.

Also in the SPS fill patterns with additional gaps significiantly reduce the density of the electron cloud. Figure 40 shows the electron-cloud build up in the SPS for the nominal case. This should be compared with Fig. 41, depicting the reduced build up obtained with six additional gaps. Note that the vertical scale in Fig. 41 is 2 orders of magnitude smaller than in Fig. 40.

In the latter fill pattern $6 \times 4 = 24$ bunches, or 33% of the total number, are missing from the 72-bunch train. A better scheme may consist of a single gap of 12 missing bunches at the center of the train, since this reduces the bunch number by only 17%. However, according to Fig.

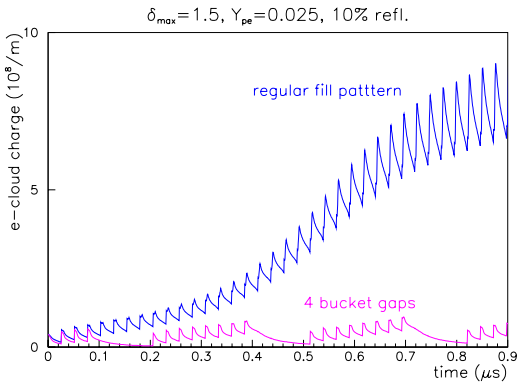

Figure 39: Suppression of charge build-up by gaps in the LHC bunch train; here a gap of 4 missing bunches is added after every 8 bunches.

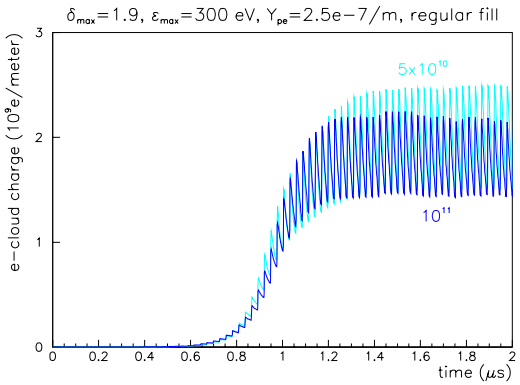

Figure 40: Electron cloud build up in the SPS for bunch populations of $N_b = 5 \times 10^{10}$ and 10^{11} (almost no difference) and regular fill. Other parameters: $\delta_{\max} = 1.9$, $Y_{pe} = 2.5 \times 10^{-7}$ m^{-1} (50 nTorr), $\epsilon_{\max} = 300$ eV, $R = 1$.

Table 3: Heat load reduction in LHC dipole with additional six gaps in the train

$\delta_{\max}$	regular fill	six gaps per train
1.1	41 mW/m	16 mW/m
1.3	222 mW/m	26 mW/m
1.5	564 mW/m	60 mW/m
2.3	5000 mW/m	890 mW/m

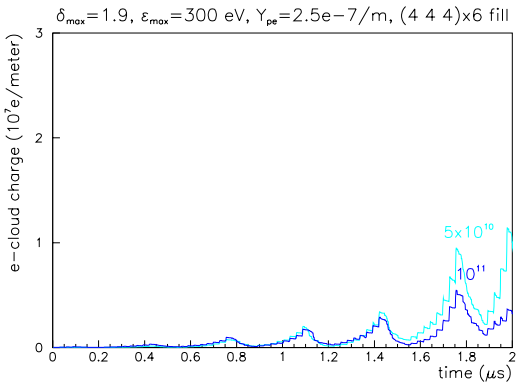

Figure 41: Electron cloud build up in the SPS for bunch populations of $N_b = 5 \times 10^{10}$ and 10^{11} and a fill pattern of 6× (4 bunches, 4 empty buckets, 4 bunches). Other parameters: $\delta_{\max} = 1.9$, $Y_{pe} = 2.5 \times 10^{-7}$ m^{-1} (50 nTorr), $\epsilon_{\max} = 300$ eV, $R = 1$.

42, for $\delta_{\max} = 1.9$ this scheme is much less effective, and the electron cloud density almost approaches the values for the nominal case. Nevertheless, the single gap does have a positive effect for lower secondary emission yields, as is illustrated in Fig. 43 for $\delta_{\max} = 1.7$.

Each of the last set of pictures presented curves for both the design intensity of $N_b = 10^{11}$ protons per bunch and for $N_b = 5 \times 10^{10}$. Somewhat surprisingly, in all cases the electron-cloud density is slightly higher for the smaller bunch population. This is possibly related to the position of the vertical stripes with maximum secondary emission yield.

As a third option, the electron-cloud build up is also slowed down by low-intensity 'satellite' bunches [32]. These are bunches which follow a few ns behind the main bunches and enhance the electron loss rate in the inter-bunch gaps [33]. Figure 44 demonstrates that satellites lagging by 3 ns completely suppress the growth of the SPS electron cloud for a satellite bunch population of $N_{\rm sat} \approx 10^{10}$. Satellite bunches of this kind can be generated by rf manipulation [34].

4 SUMMARY AND CONCLUSIONS

The electron cloud effects depend on properties of the vacuum chamber, primarily on the maximum secondary emission yield $\delta_{\max}$, the energy of maximum secondary emission $\epsilon_{\max}$, and, in case of the LHC, also on the reflectivity R, and the primary photoemission yield Y_{pe}. Our simulations indicate that the critical yield of exponential electron-cloud build up is $\delta_{\rm crit} \approx 1.3$ for both LHC and SPS. The SPS observations are consistent with our simulations of the electron cloud build up, if we choose $\delta_{\max} \approx 1.9$.

The electron cloud causes a number of undesirable effects, such as pressure rise, slow multibunch instability, single-bunch beam break up, and, for the LHC, heat load. Of these, the heat load in the LHC, and the single-bunch beam break up are the two most worriesome. The heat load is largest in the field-free region. Simulations suggest that here a weak solenoid field (of about 50 G) can significantly improve the situation, and may reduce the heat by several orders of magnitude. The emittance growth due to single-bunch beam break up should depend on the rf voltage (via

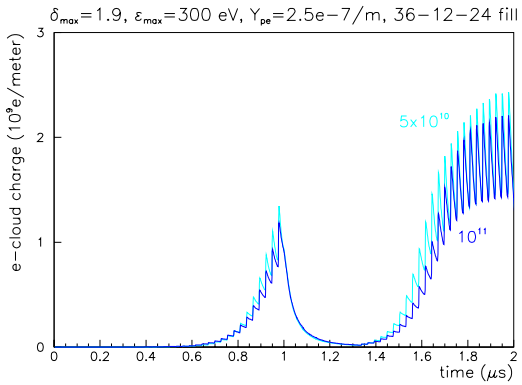

Figure 42: Electron cloud build up in the SPS for bunch populations of $N_b = 5 \times 10^{10}$ and 10^{11} and a fill pattern of 36 bunches, 12 empty buckets, 24 bunches. Other parameters: $\delta_{\max} = 1.9$, $Y_{pe} = 2.5 \times 10^{-7}$ m^{-1} (50 nTorr), $\epsilon_{\max} = 300$ eV, $R = 1$.

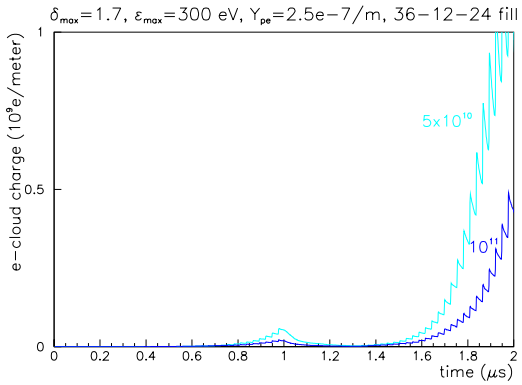

Figure 43: Electron cloud build up in the SPS for bunch populations of $N_b = 5 \times 10^{10}$ and 10^{11} and a fill pattern of 36 bunches, 12 empty buckets, 24 bunches. Other parameters: $\delta_{\max} = 1.7$, $Y_{pe} = 2.5 \times 10^{-7}$ m^{-1} (50 nTorr), $\epsilon_{\max} = 300$ eV, $R = 1$.

bunch length and synchrotron oscillation frequency) and chromaticity. Such dependencies could be explored in future machine experiments.

Finally, additional gaps in the bunch train, doubling the bunch spacing, or low-intensity satellite bunches will all suppress the electron-cloud build up and aid during surface conditioning.

5 ACKNOWLEDGEMENTS

I would like to thank G. Arduini, O. Brüning, F. Caspers, I. Collins, K. Cornelis, O. Gröbner, W. Höfle, M. Jimenez, M. Pivi, F. Ruggiero, and X. Zhang for numerous helpful discussions, and informations, and F. Ruggiero also for his support and encouragement. I am grateful to M. Furman, S. Heifets, K. Ohmi, J. Seeman, and M. Zisman for sharing many of the original ideas and simulation concepts.

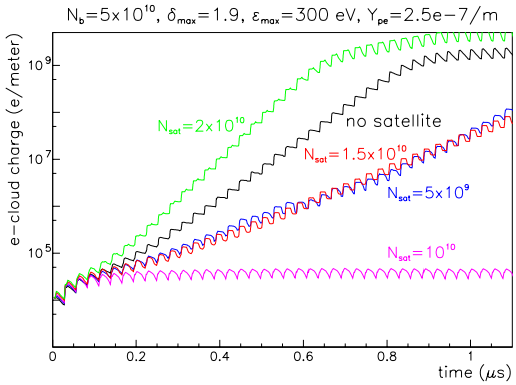

Figure 44: Electron cloud build up in the SPS for satellite bunches of various intensities, 3 ns behind the main bunches. Other parameters: $N_b = 5 \times 10^{10}$, $\delta_{\max} = 1.9$, $Y_{pe} = 2.5 \times 10^{-7}$ m^{-1} (50 nTorr), $\epsilon_{\max} = 300$ eV, $R = 1$.

6 REFERENCES

[1] O. Gröbner, 10th International Conference on High Energy Accelerators, Protvino, July (1977).

[2] For example, see comments in O. Gröbner, "Technological problems related to the cold vacuum system of the LHC", Vacuum, vol. 47, pp. 591–595 (1996).

[3] M. Izawa, Y. Sato, and T. Toyomasu, "The Vertical instability in a positron bunched beam," Phys. Rev. Lett. 74, 5044 (1995).

[4] K. Ohmi, "Beam and photoelectron interactions in positron storage rings," Phys. Rev. Lett. 75, 1526 (1995).

[5] Z.Y. Guo et al., "Study of the beam-photoelectron instability in BEPC," KEK-PREPRINT-98-23, Proc. 1st Asian Particle Accelerator Conference (APAC 98), Tsukuba, Japan (1998).

[6] M. A. Furman and G. R. Lambertson, "The electron-cloud instability in PEP-II: An update," LBL-40256, 17th IEEE Particle Accelerator Conference (PAC 97), Vancouver, Canada (1997).

[7] S. Heifets, "Study of an instability of the PEP-II positron beam: Ohmi effect and multipactoring," SLAC-PUB-6956 (1995).

[8] F. Zimmermann, 'A simulation study of electron-cloud instability and beam-induced multipacting in the LHC", LHC Project-Report 95, and SLAC-PUB-7425 (1997).

[9] O. Gröbner, "Beam induced multipacting," CERN-LHC-PROJECT-REPORT-127 17th IEEE Particle Accelerator Conference (PAC 97), Vancouver, Canada (1997).

[10] O. S. Brüning, "Simulations for the beam-induced electron cloud in the LHC beam screen with magnetic field and image charges," CERN-LHC-PROJECT-REPORT-158 (1997).

[11] O. Brüning, "Numerical Simulation for the Beam Induced Electron Cloud in the LHC", presented at EPAC98, Stockholm, LHC Project Report 190 (1998).

[12] M. Furman, “The Electron-Cloud Effect in the Arcs of the LHC”, LHC Project Report 180 (1998).

[13] F. Ruggiero, private communication (1999).

[14] M. Sands, “The Physics Of Electron Storage Rings: An Introduction,” SLAC-0121 (1970).

[15] J. Kouptsidis and G.A. Mathewson, “Reduction of the photoelectron induced gas desoprtion in the PETRA vacuum system by in situ argon glow discharge cleaning, DESY internal report, DESY 76/49, unpublished (1976).

[16] F. Zimmermann, “An Estimate of Gas Desorption in the Damping Rings of the Next Linear Collider,” Nucl. Instr. Meth. A 398, 131 (1997).

[17] V. Baglin et al., “Experimental Investigations of the Electron Cloud Key Parameters”, CERN LHC Project Report 313, presented at e^+e^- Factories ‘99, Tsukuba (1999).

[18] V. Baglin, I. R. Collins and O. Grobner, “Photoelectron yield and photon reflectivity from candidate LHC vacuum chamber materials with implications to the vacuum chamber design,” CERN LHC Project Report 206 Proc. 6th European Particle Accelerator Conference (EPAC 98), Stockholm, Sweden (1988).

[19] J.S. Berg, “Energy Gain in an Electron Cloud during the Passage of a Bunch”, CERN LHC Project Note 97 (1997).

[20] H. Seiler, “Secondary electron emission in the scanning electron microscope”, J. Appl. Phys. 54 (11) (1983).

[21] M.A. Furman and G.R. Lambertson, “The Electron Cloud Effect in the arcs of the PEP-II Positron Ring,” KEK Proceedings 97-17, p. 170, December 1997 (Proc. MBI97 workshop, KEK, Y.H. Chhin, ed.) (1997).

[22] M. Bassetti and G. A. Erskine, “Closed Expression For The Electrical Field Of A Two-Dimensional Gaussian Charge,” CERN-ISR-TH/80-06 (1980).

[23] M. Furman, “Comments on the Electron-Cloud Effect in the LHC Dipole Bending Magnets”,

[24] G. Stupakov, “Photoelectrons and Multipacting in the LHC: Electron Cloud Build-Up”, LHC Project Report 141 (1997).

[25] L. Vos, “Electron Cloud: an Analytic View”, LHC Project Note 150 (1998).

[26] O. Gröbner, private communication (1999).

[27] W. Hoefle, private communication (1999).

[28] I. Collins, private communication (1999).

[29] A.W. Chao, “Physics of Collective Beam Instabilities in High Energy Accelerators”, Wiley (1993).

[30] F. Zimmermann, “Electron-Cloud Studies for the Low-Energy Ring of KEKB,” CERN SL-Note-2000-004 AP (2000).

[31] T. Raubenheimer and F. Zimmermann, “A Fast Beam-Ion Instability in Linear Accelerators and Storage Rings,” SLAC-PUB 95-6740, Phys. Rev. **E52** 5487 (1995).

[32] O. Brüning, *et al.*, “Electron-Cloud and Beam Scrubbing in the LHC,” presented at IEEE PAC99, New York (1999).

[33] Satellite bunches were first proposed by F. Ruggiero.

[34] T. Bohl, presented at Chamonix 2000, these proceedings (2000).